SIAM J. SCI. COMPUT.
Vol. 20, No. 3, pp. 858–877

A NUMERICAL STUDY OF THE AXISYMMETRIC COUETTE–TAYLOR PROBLEM USING A FAST HIGH-RESOLUTION SECOND-ORDER CENTRAL SCHEME*

RAZ KUPFERMAN†

Abstract. We present a numerical study of the axisymmetric Couette–Taylor problem using a finite difference scheme. The scheme is based on a staggered version of a second-order central-differencing method combined with a discrete Hodge projection. The use of central-differencing operators obviates the need to trace the characteristic flow associated with the hyperbolic terms. The result is a simple and efficient scheme which is readily adaptable to other geometries and to more complicated flows. The scheme exhibits competitive performance in terms of accuracy, resolution, and robustness. The numerical results agree accurately with linear stability theory and with previous numerical studies.

Key words. central difference schemes, incompressible flow, Couette–Taylor problem

AMS subject classifications. 65M06, 76U05, 76E10

PII. S1064827597318009

1. Introduction.

Despite several decades of progress, the accurate computation of flow problems is still a challenging task. Sophisticated schemes have been designed to cope with a variety of physical problems. Sophisticated methods are inherently difficult to apply, especially if they require additional adaptation for each specific problem. This is an obstacle that often prevents the use of modern methods in practical applications, e.g., in mechanical or chemical engineering. It is the purpose of this paper to show the applicability of a simple, easy-to-implement, computationally efficient, and readily generalizable scheme for flow problems. The realization and performance of the scheme are demonstrated on the well-studied axisymmetric Couette–Taylor system.

Many modern finite difference methods used in flow computations are based on the Godunov paradigm, where the time evolution of a piecewise-polynomial approximation of the flow field is sought. Typically, this piecewise-polynomial approximation is reconstructed from its cell averages. In this context, we distinguish between two main classes of methods: *upwind* and *central* methods.

Upwind schemes evaluate averages over the same computational cells that were used to construct the initial piecewise-polynomial elements. The computation of the time evolution of the flow field requires the evaluation of fluxes along the cell interfaces, i.e., along the discontinuous breakpoints. Consequently, the characteristic speeds along such interfaces must be taken into account. Special attention is required at those interfaces in which there is a combination of forward- and backward-going waves, where it is necessary to decompose the "Riemann fan" and determine the separate contribution of each component by tracing the "direction of the wind." It is the need to trace characteristic fans, using exact or approximate Riemann solvers, that greatly complicates the upwind algorithms. The first-order Godunov upwind scheme

*Received by the editors March 3, 1997; accepted for publication (in revised form) July 28, 1997; published electronically October 20, 1998. This work was supported by the U.S. Department of Energy under contract DE-AC03-76SF-00098.

http://www.siam.org/journals/sisc/20-3/31800.html

†Mathematics Department, Lawrence Berkeley National Laboratory, 1 Cyclotron Road, 50A-2152, Berkeley, CA 94720 (raz@math.lbl.gov).

[9] is the forerunner for all the other Godunov-type schemes [16, 24, 11, 22, 7]. For incompressible flow, the upwind-Godunov scheme was combined with Chorin's projection technique [5] by Bell, Colella, and Glaz [2], E and Shu [8], and others. For a review, see [10, 17, 6] and the references therein.

Central schemes differ from upwind schemes in their way of calculating averages. In central schemes averages are evaluated over cells on a *staggered* grid so the breakpoints between the piecewise-polynomial elements are now *inside* the computational cells. Averages are now integrated over the entire Riemann fan, while the corresponding fluxes are evaluated at the smooth centers of the piecewise-polynomial elements. This method obviates the need for Riemann solvers resulting in simpler and faster schemes. The first-order Lax–Friedrichs (LxF) scheme [15] is the canonical example of such central schemes. Like Godunov's upwind scheme, it is based on a piecewise-constant approximation. The LxF scheme, however, introduces excessive numerical viscosity resulting in relatively poor resolution.

Modern high-resolution central schemes were introduced by Nessyahu and Tadmor (NT) [21] as a second-order sequel to the LxF scheme in one spatial dimension. The original NT scheme, which was based on a piecewise-linear approximation, yielded a considerable improvement in terms of resolution; at the same time, it retained the relatively simple form of central schemes. The NT scheme was then extended to higher orders [20] and to several spatial dimensions [12]. This and related work [25, 27] convincingly demonstrated that central schemes offer a much simpler alternative to upwind schemes while retaining a comparable resolution.

The central schemes mentioned above were introduced primarily for hyperbolic conservation laws, such as those governing compressible flow. The conservation laws for incompressible flow are additionally constrained by the incompressibility condition, which makes the dynamics nonlocal. The two-dimensional Euler equations in their vorticity formulation were treated along these lines by Levy and Tadmor, both in second- and third-order versions [18]. The resolution obtained by the latter is remarkable. However, there are two major shortcomings to using the vorticity formulation: boundary conditions are hard to formulate, and the method is not easily extended to three spatial dimensions.

These problems were resolved by Kupferman and Tadmor (KT) [14], where incompressible flow was calculated in a velocity formulation based on the projection method. The new scheme was tested on the classical doubly periodic shear layer and on longitudinal flow in a channel. The performance was compared to that of an upwind scheme. The two methods are comparable in accuracy and resolution. The new scheme was further found to be immune to the formation of spurious vortical structures [3].

The simplicity, accuracy, and resolution of the KT scheme make it a promising candidate for tackling new and more complex problems, for example, in the domain of non-Newtonian fluids [13]. For that, it has to be generalized in several aspects: (i) treatment of more complex equations (e.g., coupling to constitutive equations); (ii) adaptation to various geometries and coordinate systems; and (iii) systematic treatment of boundary conditions. The last point was addressed only in a partially satisfactory way in [14].

In this paper, we apply the KT method on the axisymmetric Couette–Taylor problem. This particular problem was chosen for several reasons. First, it involves cylindrical coordinates and thus demonstrates how to implement the staggered central approach for non-Cartesian coordinates. Second, it offers a challenge to the numerical

treatment of boundary conditions because the centrifugal forces constantly push the fluid toward the outer cylinder. Finally, the availability of data and analytical results allows an extensive test of the numerical results.

We find that the generalization to cylindrical coordinates fits very naturally into the staggered central-differencing methodology. It requires the formulation of the equations of motion in the appropriate conservative form; averages have to be calculated with the radius-dependent weight associated with the cylindrical coordinates.

The treatment of boundary conditions demands additional attention due to the alternation between two different grids. It follows the same lines as in the basic scheme, except for adaptations resulting from the existence of half-cells and for the use of one-sided stencils to calculate derivatives.

We investigate the Couette–Taylor problem for the regime of parameters in which axisymmetric solutions are relevant: azimuthal flow and steady Taylor vortices. We compare our results with the predictions of linear stability theory and find excellent agreement. The results are accurate even for a relatively coarse grid.

This paper is organized as follows. In section 2 we present the equations of motion, both in their advective and conservative form. The latter is the starting point for the central scheme approach. In section 3 we describe the numerical scheme. For clarity, we divide the presentation between the treatment of interior and perimeter cells. The numerical results are described in section 4. A short discussion is presented in section 5.

2. The axisymmetric Navier–Stokes equations. A circular Couette cell consists of a fluid confined between two concentrically rotating cylinders. The geometry imposes the natural choice of cylindrical coordinates: let $\mathbf{x} = (r, \theta, z)$ and $\mathbf{u} = (u, v, w)$ denote the radial, azimuthal, and axial components of the coordinates and the flow field respectively. We consider here axisymmetric flow; the flow field does not depend on the azimuthal coordinate θ. The Navier–Stokes equations which govern the flow of Newtonian fluids are

$$
\begin{aligned}
\frac{\partial u}{\partial t} &= -u\frac{\partial u}{\partial r} - w\frac{\partial u}{\partial z} + \frac{v^2}{r} - \frac{\partial p}{\partial r} + \bar{\nu}\left[\frac{\partial}{\partial r}\left(\frac{1}{r}\frac{\partial}{\partial r}(ru)\right) + \frac{\partial^2 u}{\partial z^2}\right], \\
\frac{\partial v}{\partial t} &= -u\frac{\partial v}{\partial r} - w\frac{\partial v}{\partial z} - \frac{uv}{r} + \bar{\nu}\left[\frac{\partial}{\partial r}\left(\frac{1}{r}\frac{\partial}{\partial r}(rv)\right) + \frac{\partial^2 v}{\partial z^2}\right], \qquad (1) \\
\frac{\partial w}{\partial t} &= -u\frac{\partial w}{\partial r} - w\frac{\partial w}{\partial z} - \frac{\partial p}{\partial z} + \bar{\nu}\left[\frac{1}{r}\frac{\partial}{\partial r}\left(r\frac{\partial w}{\partial r}\right) + \frac{\partial^2 w}{\partial z^2}\right],
\end{aligned}
$$

with the incompressibility condition

$$
\frac{1}{r}\frac{\partial}{\partial r}(ru) + \frac{\partial w}{\partial z} = 0, \qquad (2)
$$

where $p(\mathbf{x}, t)$ is the pressure field and $\bar{\nu}$ is the kinematic viscosity.

As originally explained by Rayleigh [23], the Couette–Taylor instability results from a radial stratification of the angular momentum density $\ell = rv$. The special role of angular momentum suggests a change of variables, replacing the equation for v by an equivalent equation for ℓ. The substitution is straightforward.

The central scheme approach is based on the dual nature of the equations of motion, which can be formulated both in advective form (1) and in (partially) conservative form. The equivalence of the two representations is guaranteed by the incompressibility condition (2). Unlike in Cartesian coordinates, it is not possible to obtain

a fully conservative system of equations in cylindrical coordinates. In the context of conservative systems there are additional terms which play the role of "sources" (e.g., the centrifugal force).

A scalar field $\psi(\mathbf{x},t)$ is said to satisfy a hyperbolic conservation law if its equation of motion is of the general form $\frac{\partial\psi}{\partial t} = \nabla\cdot\mathbf{j}(\psi)$, where $\mathbf{j}(\psi)$ is the flux associated with the conserved quantity ψ. In axisymmetric cylindrical coordinates, the representation of the divergence operator is $(\frac{1}{r}\frac{\partial}{\partial r}r, 0, \frac{\partial}{\partial z})$, so hyperbolic conservation laws assume the specific form

$$\frac{\partial\psi}{\partial t} = \frac{1}{r}\frac{\partial}{\partial r}rj_r + \frac{\partial}{\partial z}j_z. \tag{3}$$

It is now a matter of simple algebra to rewrite (1) in the appropriate conservation form:

$$\begin{aligned}
\frac{\partial u}{\partial t} &= \frac{1}{r}\frac{\partial}{\partial r}r\left[-u^2+\bar\nu\frac{\partial u}{\partial r}\right] + \frac{\partial}{\partial z}\left[-wu+\bar\nu\frac{\partial u}{\partial z}\right] + \left[-\frac{\partial p}{\partial r}+\frac{\ell^2}{r^3}-\bar\nu\frac{u}{r^2}\right],\\
\frac{\partial \ell}{\partial t} &= \frac{1}{r}\frac{\partial}{\partial r}r\left[-u\ell+\bar\nu\frac{\partial \ell}{\partial r}-2\bar\nu\frac{\ell}{r}\right] + \frac{\partial}{\partial z}\left[-w\ell+\bar\nu\frac{\partial \ell}{\partial z}\right],\\
\frac{\partial w}{\partial t} &= \frac{1}{r}\frac{\partial}{\partial r}r\left[-uw+\bar\nu\frac{\partial w}{\partial r}\right] + \frac{\partial}{\partial z}\left[-w^2+\bar\nu\frac{\partial w}{\partial z}\right] + \left[-\frac{\partial p}{\partial z}\right].
\end{aligned} \tag{4}$$

The purely conservative equation for ℓ reflects the fact that angular momentum is conserved inside the cell.

We next specify the boundary conditions. At the rigid walls, $r = R_{in}$ and $r = R_{out}$, the no-slip conditions imply that the velocity of the fluid equals that of the rotating cylinders. If Ω_{in} and Ω_{out} denote the angular velocities of the inner and the outer cylinders, respectively, then the boundary conditions are

$$\begin{aligned}
&u(R_{in}) = u(R_{out}) = w(R_{in}) = w(R_{out}) = 0,\\
&\ell(R_{in}) = \Omega_{in}R_{in}^2, \qquad \ell(R_{out}) = \Omega_{out}R_{out}^2.
\end{aligned} \tag{5}$$

For the axial axis we will assume for convenience periodic boundary conditions. This has little effect on the solution provided that the height of the cylinders is large compared to the characteristic wavelength of the flow pattern. This condition is met in all our calculations.

The number of independent parameters may be reduced by introducing dimensionless variables: we measure length in terms of intercylindrical gap units, $R_{out}-R_{in}$, and time in terms of the rotation period of the inner cylinder, $1/\Omega_{in}$. The velocity field is then expressed in units of $\Omega_{in}(R_{out}-R_{in})$ and viscosity in units of $\Omega_{in}(R_{out}-R_{in})^2$. We will denote the dimensionless viscosity by ν. In these units, the boundary conditions for the angular momentum read

$$\ell(r_L) = \frac{\eta^2}{(1-\eta)^2} \qquad \text{and} \qquad \ell(r_R) = \frac{\omega}{(1-\eta)^2}, \tag{6}$$

where

$$r_L = \frac{\eta}{1-\eta} \qquad \text{and} \qquad r_R = \frac{1}{1-\eta} \tag{7}$$

denote the cylindrical radii, $\eta \equiv R_{in}/R_{out}$, and $\omega \equiv \Omega_{out}/\Omega_{in}$. Thus the model includes only three independent parameters: η, ω, and ν.

Following [1], we further define the Reynolds numbers associated with the inner and the outer cylinders as

$$\mathcal{R}_{in} \equiv \frac{R_{in}(R_{out}-R_{in})\Omega_{in}}{\bar{\nu}} = \frac{\eta}{\nu(1-\eta)} \tag{8}$$

and

$$\mathcal{R}_{out} \equiv \frac{R_{out}(R_{out}-R_{in})\Omega_{out}}{\bar{\nu}} = \frac{\omega}{\nu(1-\eta)}. \tag{9}$$

For all values of the parameters, these equations have an azimuthal stationary solution, known as Couette flow:

$$u(r) = w(r) = 0, \qquad \ell(r) = Ar^2 + B, \tag{10}$$

where the coefficients A and B are given by

$$A = \frac{\omega-\eta^2}{1-\eta^2} \qquad \text{and} \qquad B = \frac{(1-\omega)\eta^2}{(1-\eta)^2(1-\eta^2)}. \tag{11}$$

3. The numerical scheme. We now turn to the presentation of the central scheme. We start by describing the scheme for interior cells in section 3.1. We treat the boundary cells in section 3.2.

3.1. Interior cells. The computational grid consists of rectangular cells of size Δr and Δz; at time level t^n these cells $\mathcal{C}_{i,j}$ are centered at $(r_i = r_L + i\Delta r, z_j = j\Delta z)$, with $i = 0,\ldots,M-1$ and $j = 0,\ldots,N-1$. The velocity field (u,ℓ,w) is represented by the *point values* at the cells' centers, $\mathbf{u}^n_{i,j} = (u^n_{i,j}, \ell^n_{i,j}, w^n_{i,j})$. The pressure gradient ∇p is assumed to be given at the former midtime $t^{n-\frac{1}{2}}$, and is also represented by its point values $(G_r p^{n-\frac{1}{2}}_{i,j}, 0, G_z p^{n-\frac{1}{2}}_{i,j})$.

3.1.1. Piecewise-linear reconstruction. The first step is a piecewise-polynomial reconstruction of the velocity field to recover point values throughout the cell. Second-order accuracy is guaranteed by a piecewise-linear reconstruction, which takes the form

$$\mathbf{u}^n(r,z) = \mathbf{u}^n_{i,j} + \mathbf{u}'_{i,j}(r-r_i) + \mathbf{u}\backprime_{i,j}(z-z_j), \qquad r,z \in \mathcal{C}_{i,j}, \tag{12}$$

where $\mathbf{u}'_{i,j}$ and $\mathbf{u}\backprime_{i,j}$ approximate the r- and z-derivatives at the cells' centers (r_i, z_j), respectively. In general, the recipe for constructing such derivatives requires nonlinear limiters in order to prevent the formation of nonlinear oscillations [16, 26, 19]. As reported in [14], the central scheme proves to be quite robust against the formation and the propagation of spurious oscillations. We therefore calculate $\mathbf{u}'_{i,j}$ and $\mathbf{u}\backprime_{i,j}$ using simple central differences

$$\mathbf{u}'_{i,j} = D^0_r \mathbf{u}^n_{i,j} \qquad \text{and} \qquad \mathbf{u}\backprime_{i,j} = D^0_z \mathbf{u}^n_{i,j}, \tag{13}$$

where $D^0_{r,z}$ denote the r- and z- central difference operators.

3.1.2. Calculation of the provisional field. The second step is to evolve the piecewise-linear approximation to the next time level t^{n+1}. The time evolution of the flow field is given by (4), subject to the incompressibility constraint imposed by (2). The latter determines the pressure $p(\mathbf{x}, t)$, which could be viewed as a Lagrange multiplier.

We follow the projection method [5]. Consider the following second-order *temporal* discretization of the equations of motion:

$$\frac{\mathbf{u}^{n+1} - \mathbf{u}^n}{\Delta t} = \left[-(\mathbf{u}\cdot\nabla)\mathbf{u} + \nu\nabla^2\mathbf{u}\right]^{n+\frac{1}{2}} - \nabla p^{n+\frac{1}{2}}, \tag{14}$$

where the updated flow field satisfies the incompressibility condition

$$\nabla\cdot\mathbf{u}^{n+1} = 0. \tag{15}$$

The Hodge decomposition theorem states that any vector field $\mathbf{u}$ can be uniquely decomposed into a divergence-free component which is tangential to the domain boundaries, and an irrotational component. Let $\mathbb{P}$ denote the operator which projects a vector field onto the space of divergence-free fields. Then (14) and (15) can be replaced by the equivalent set of equations

$$\mathbf{u}^{n+1} = \mathbb{P}\mathbf{u}^* \tag{16}$$

and

$$\nabla p^{n+\frac{1}{2}} = \nabla p^{n-\frac{1}{2}} + \frac{1}{\Delta t}(\mathbb{I} - \mathbb{P})\mathbf{u}^*, \tag{17}$$

where

$$\mathbf{u}^* \equiv \mathbf{u}^n + \Delta t\left[-(\mathbf{u}\cdot\nabla)\mathbf{u} + \nu\nabla^2\mathbf{u}\right]^{n+\frac{1}{2}} - \Delta t\,\nabla p^{n-\frac{1}{2}} \tag{18}$$

is a *provisional* flow field.

In other words, lacking the knowledge of ∇p at the midtime $t^{n+\frac{1}{2}}$, we approximate it by its value at the former midtime $t^{n-\frac{1}{2}}$. The result is a provisional field $\mathbf{u}^*$ which differs from the actual updated flow field $\mathbf{u}^{n+1}$ by the gradient of a scalar function, $\Delta t\,\nabla(p^{n+\frac{1}{2}} - p^{n-\frac{1}{2}})$. Hence, $\mathbf{u}^{n+1}$ is the projection of the provisional field, while the irrotational residual can be used to update the pressure gradient at time $t^{n+\frac{1}{2}}$. (The provisional field in Chorin's original method did not include the ∇p term, resulting in a first-order scheme. This addition is due to Bell, Colella, and Glaz [2].)

We now turn to the computation of the provisional field $\mathbf{u}^*$. Its time evolution can be cast in the general form

$$\frac{\partial\mathbf{u}^*}{\partial t} = \frac{1}{r}\frac{\partial}{\partial r}r\mathbf{F}(\mathbf{u}^*, r) + \frac{\partial}{\partial z}\mathbf{G}(\mathbf{u}^*, r) + \mathbf{S}(\mathbf{u}^*, r), \tag{19}$$

where $\mathbf{F}(\mathbf{u}^*, r)$ and $\mathbf{G}(\mathbf{u}^*, r)$ denote the r- and z-components of the *fluxes*, and $\mathbf{S}(\mathbf{u}^*, r)$ is the *source* term that includes all terms which do not fit into the conservation form.

Specifically,

$$\mathbf{F}(\mathbf{u}^*, r) = \begin{pmatrix} -{u^*}^2 + \nu \dfrac{\partial u^*}{\partial r} \\ -u^* l^* + \nu \dfrac{\partial l^*}{\partial r} - 2\nu \dfrac{l^*}{r} \\ -u^* w^* + \nu \dfrac{\partial w^*}{\partial r}, \end{pmatrix} \qquad \mathbf{G}(\mathbf{u}^*, r) = \begin{pmatrix} -w^* u^* + \nu \dfrac{\partial u^*}{\partial z} \\ -w^* l^* + \nu \dfrac{\partial l^*}{\partial z} \\ -{w^*}^2 + \nu \dfrac{\partial w^*}{\partial z} \end{pmatrix},$$

$$\mathbf{S}(\mathbf{u}^*, r) = \begin{pmatrix} \dfrac{{l^*}^2}{r^3} - \nu \dfrac{u^*}{r^2} - \dfrac{\partial p}{\partial r} \\ 0 \\ -\dfrac{\partial p}{\partial z} \end{pmatrix}. \tag{20}$$

At time t^n, the provisional field $\mathbf{u}^*$ equals the actual flow field $\mathbf{u}^n$. We evolve $\mathbf{u}^*$ to time t^{n+1} by first calculating its cell averages $\bar{\mathbf{u}}^*$ over the *staggered* grid cells $\mathcal{C}_{i+\frac{1}{2},j+\frac{1}{2}}$. Note that in axisymmetric cylindrical coordinates, spatial averages are weighted in proportion to the radius r. These cell averages can be expressed as integrals over the control box, $\mathcal{C}_{i+\frac{1}{2},j+\frac{1}{2}} \times [t^n, t^{n+1}]$:

$$\begin{aligned} \bar{\mathbf{u}}^*_{i+\frac{1}{2},j+\frac{1}{2}} &\equiv \fint_{\mathcal{C}_{i+\frac{1}{2},j+\frac{1}{2}}} r\, dr\, dz\, \mathbf{u}^* \\ &= \fint_{\mathcal{C}_{i+\frac{1}{2},j+\frac{1}{2}}} r\, dr\, dz\, \mathbf{u}^n + \int_{t_n}^{t_{n+1}} dt \fint_{\mathcal{C}_{i+\frac{1}{2},j+\frac{1}{2}}} r\, dr\, dz\, \frac{\partial \mathbf{u}^*}{\partial t}. \end{aligned} \tag{21}$$

The computational grid and the control box are sketched in Fig. 1, with the vertical axis representing time. The notation $\fint_\Omega = \frac{1}{\Omega}\int_\Omega$ is for normalized integrals, scaled by their area, length, etc.; here, for example, the volume of the annulus whose cross section is the staggered cell $\mathcal{C}_{i+\frac{1}{2},j+\frac{1}{2}}$ is $r_{i+\frac{1}{2}} \Delta r \Delta z$.

The first term in (21) is a simple average of the piecewise-linear function $\mathbf{u}^n$ over the bottom of the integration box shown in Fig. 1. It involves contributions from the four intersecting cells $\mathcal{C}_{i,j}$, $\mathcal{C}_{i+1,j}$, $\mathcal{C}_{i,j+1}$, and $\mathcal{C}_{i+1,j+1}$. A straightforward computation yields

$$\begin{aligned} \fint_{\mathcal{C}_{i+\frac{1}{2},j+\frac{1}{2}}} d\mathbf{r}\, \mathbf{u}^n = \mu_r^+ \mu_z^+ \mathbf{u}^n_{i,j} + \frac{\Delta r^2}{8 r_{i+\frac{1}{2}}} D_r^+ \mu_z^+ \mathbf{u}^n_{i,j} - \frac{\Delta r^2}{8} D_r^+ \mu_z^+ \mathbf{u}'_{i,j} \\ - \frac{\Delta r^2}{24 r_{i+\frac{1}{2}}} \mu_r^+ \mu_z^+ \mathbf{u}'_{i,j} - \frac{\Delta z^2}{8} D_z^+ \mu_r^+ \mathbf{u}\backprime_{i,j}. \end{aligned} \tag{22}$$

The notation here is defined as follows. $D_r^+ \mathbf{u}_{i,\cdot} \equiv (\mathbf{u}_{i+1,\cdot} - \mathbf{u}_{i,\cdot})/\Delta r$ and $\mu_r^+ \mathbf{u}_{i,\cdot} \equiv \frac{1}{2}(\mathbf{u}_{i+1,\cdot} + \mathbf{u}_{i,\cdot})$ denote forward differences and forward averages in the r-direction, respectively. The meaning of the related operators D_r^-, μ_r^-, D_z^+, D_z^-, μ_z^+, and μ_z^- is self-evident.

We now discuss the integration over the fluxes $\mathbf{F}$ and $\mathbf{G}$. This is where the virtues of the conservation form enter. For example, the integral $\int r\, dr$ over the flux $\mathbf{F}$ is simple to perform and equals the difference between the fluxes at r_{i+1} and r_i. This flux difference is then integrated over the two interfaces of the control box

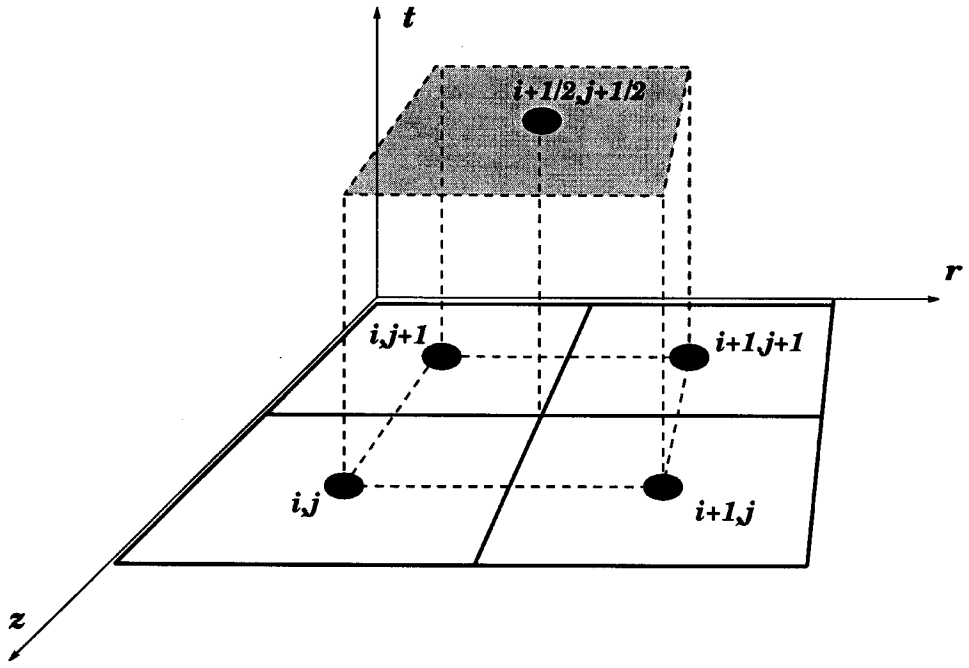

FIG. 1. *The computational grid. At time t^n, the data refer to the cells $\mathcal{C}_{i,j}$ centered at $(i\,\Delta r, j\,\Delta z)$. At time t^{n+1}, staggered cells $\mathcal{C}_{i+\frac{1}{2},j+\frac{1}{2}}$ are used.*

(Fig. 2):

$$\int_{t_n}^{t_{n+1}} dt \oint_{\mathcal{C}_{i+\frac{1}{2},j+\frac{1}{2}}} r\,dr\,dz\,\frac{1}{r}\frac{\partial}{\partial r} r\mathbf{F}(r,z,t) = \frac{1}{r_{i+\frac{1}{2}}} D_r^+ \int_{t_n}^{t_{n+1}} dt \oint_{J_{j+\frac{1}{2}}} dz\, r_i \mathbf{F}(r_i,z,t), \tag{23}$$

where $J_{j+\frac{1}{2}}$ refers to the segment of length Δz centered at $z_{j+\frac{1}{2}}$.

So far, the procedure is exact. Approximations are required when we integrate $(r\mathbf{F})$ over the interfaces of the control box. For second-order accuracy, the integral over z is approximated by the second-order trapezoidal rule. The integral over time is approximated by the midpoint rule. For that, we need an approximation of the fields at time $t^{n+\frac{1}{2}}$ at the centers of the cells $\mathcal{C}_{i,j}$. $\mathbf{u}_{i,j}^{n+\frac{1}{2}}$ can be obtained by a first-order explicit predictor step.

A slightly different procedure is adopted for the temporal integration of the viscosity terms νu_r, etc. Stability considerations favor instead the implicit Crank–Nicholson scheme, which consists of an averaging between values at times t^n and t^{n+1}.

The integration over the flux $\mathbf{G}$ follows the same lines. There remains the source term $\mathbf{S}(\mathbf{u}, r)$ for which the spatial integration can be approximated by a second-order averaging over the four corners:

$$\oint_{\mathcal{C}_{i+\frac{1}{2},j+\frac{1}{2}}} r\,dr\,dz\,\mathbf{S}(r,z,t) \simeq \frac{1}{r_{i+\frac{1}{2}}} \mu_r^+ \mu_z^+ \left[r\mathbf{S}(r_i, z_j, t)\right]. \tag{24}$$

The time integration is again approximated by the midpoint rule.

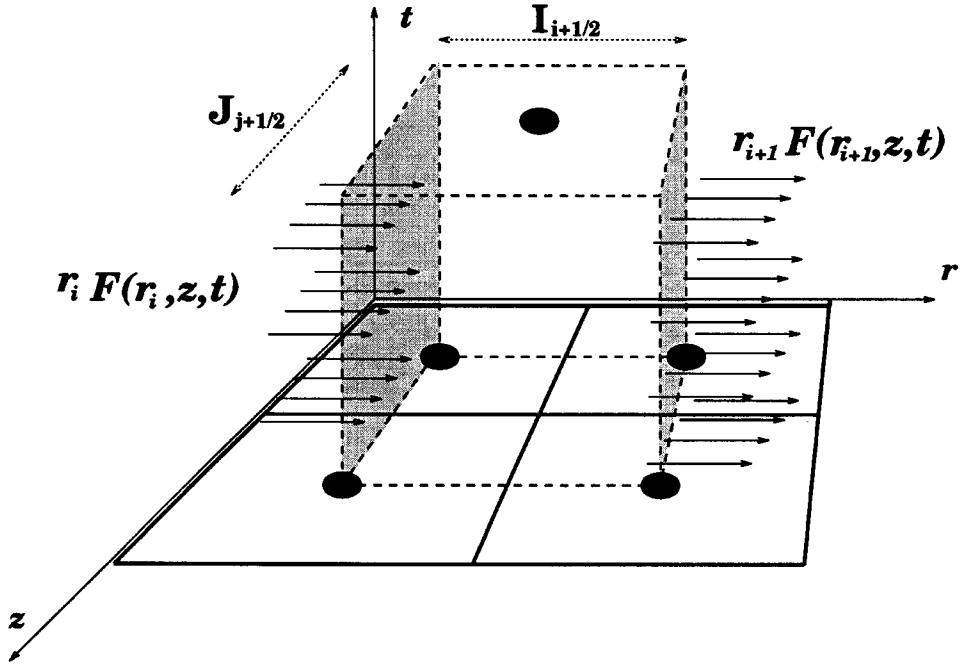

FIG. 2. *Integration over the flux* $\mathbf{F}$*: the integral over the control box* $\mathcal{C}_{i+\frac{1}{2},j+\frac{1}{2}} \times [t^n, t^{n+1}]$ *reduces to the flux difference* $\Delta r\, D_r^+(r\mathbf{F})$*, integrated over the sides* $J_{j+\frac{1}{2}} \times [t^n, t^{n+1}]$ *(shaded areas).*

Thus the calculation of the cell averages $\bar{\mathbf{u}}^*_{i+\frac{1}{2},j+\frac{1}{2}}$ consists of a predictor step

$$u^{n+\frac{1}{2}}_{i,j} = u^n_{i,j} + \frac{\Delta t}{2}\left\{-u^n_{i,j}u'_{i,j} - w^n_{i,j}u\backprime_{i,j} + \frac{(\ell^n_{i,j})^2}{r_i^3} - G_r p^{n-\frac{1}{2}}_{i,j} + \nu\left(\frac{u'_{i,j}}{r_i} - \frac{u^n_{i,j}}{r_i^2}\right) + \nu\left(\frac{\partial^2 u^n_{i,j}}{\partial r^2} + \frac{\partial^2 u^n_{i,j}}{\partial z^2}\right)\right\},$$

$$\ell^{n+\frac{1}{2}}_{i,j} = \ell^n_{i,j} + \frac{\Delta t}{2}\left\{-u^n_{i,j}\ell'_{i,j} - w^n_{i,j}\ell\backprime_{i,j} - \nu\frac{\ell'_{i,j}}{r_i} + \nu\left(\frac{\partial^2 \ell^n_{i,j}}{\partial r^2} + \frac{\partial^2 \ell^n_{i,j}}{\partial z^2}\right)\right\},$$

$$w^{n+\frac{1}{2}}_{i,j} = w^n_{i,j} + \frac{\Delta t}{2}\left\{-u^n_{i,j}w'_{i,j} - w^n_{i,j}w\backprime_{i,j} - G_z p^{n-\frac{1}{2}}_{i,j} + \nu\frac{w'_{i,j}}{r_i} + \nu\left(\frac{\partial^2 w^n_{i,j}}{\partial r^2} + \frac{\partial^2 w^n_{i,j}}{\partial z^2}\right)\right\}, \tag{25}$$

followed by a corrector step

$$\left[1 - \frac{\nu\Delta t}{2}\nabla^2\right]\bar{u}^*_{i+\frac{1}{2},j+\frac{1}{2}} = \mu_r^+\mu_z^+ u^n_{i,j} + \frac{\Delta r^2}{8r_{i+\frac{1}{2}}}D_r^+\mu_z^+ u^n_{i,j} - \frac{\Delta r^2}{8}D_r^+\mu_z^+ u'_{i,j} - \frac{\Delta r^2}{24 r_{i+\frac{1}{2}}}\mu_r^+\mu_z^+ u'_{i,j} - \frac{\Delta z^2}{8}D_z^+\mu_r^+ u\backprime_{i,j} + \frac{\Delta t}{r_{i+\frac{1}{2}}}D_r^+\mu_z^+\left\{r_i\left[-(u^{n+\frac{1}{2}}_{i,j})^2 + \frac{\nu}{2}u'_{i,j}\right]\right\}$$

$$+\frac{\Delta t}{r_{i+\frac{1}{2}}}D_z^+\mu_r^+\left\{r_i\left[-w_{i,j}^{n+\frac{1}{2}}u_{i,j}^{n+\frac{1}{2}}+\frac{\nu}{2}u_{i,j}^{\backslash}\right]\right\}$$
$$+\frac{\Delta t}{r_{i+\frac{1}{2}}}\mu_r^+\mu_z^+\left\{r_i\left[\frac{\left(\ell_{i,j}^{n+\frac{1}{2}}\right)^2}{r_i^3}-\nu\frac{u_{i,j}^{n+\frac{1}{2}}}{r_i^2}-G_r p_{i,j}^{n-\frac{1}{2}}\right]\right\},$$

$$\left[1-\frac{\nu\Delta t}{2}\nabla^2\right]\bar{l}^*_{i+\frac{1}{2},j+\frac{1}{2}}=\mu_r^+\mu_z^+\ell_{i,j}^n+\frac{\Delta r^2}{8r_{i+\frac{1}{2}}}D_r^+\mu_z^+\ell_{i,j}^n-\frac{\Delta r^2}{8}D_r^+\mu_z^+\ell'_{i,j}$$
$$-\frac{\Delta r^2}{24r_{i+\frac{1}{2}}}\mu_r^+\mu_z^+\ell'_{i,j}-\frac{\Delta z^2}{8}D_z^+\mu_r^+\ell_{i,j}^{\backslash}$$
$$+\frac{\Delta t}{r_{i+\frac{1}{2}}}D_r^+\mu_z^+\left\{r_i\left[-u_{i,j}^{n+\frac{1}{2}}\ell_{i,j}^{n+\frac{1}{2}}+\frac{\nu}{2}\ell'_{i,j}-2\nu\frac{\ell_{i,j}^{n+\frac{1}{2}}}{r_i}\right]\right\}$$
$$+\frac{\Delta t}{r_{i+\frac{1}{2}}}D_z^+\mu_r^+\left\{r_i\left[-w_{i,j}^{n+\frac{1}{2}}\ell_{i,j}^{n+\frac{1}{2}}+\frac{\nu}{2}\ell_{i,j}^{\backslash}\right]\right\},$$

$$\left[1-\frac{\nu\Delta t}{2}\nabla^2\right]\bar{w}^*_{i+\frac{1}{2},j+\frac{1}{2}}=\mu_r^+\mu_z^+w_{i,j}^n+\frac{\Delta r^2}{8r_{i+\frac{1}{2}}}D_r^+\mu_z^+w_{i,j}^n-\frac{\Delta r^2}{8}D_r^+\mu_z^+w'_{i,j}$$
$$-\frac{\Delta r^2}{24r_{i+\frac{1}{2}}}\mu_r^+\mu_z^+w'_{i,j}-\frac{\Delta z^2}{8}D_z^+\mu_r^+w_{i,j}^{\backslash}$$
$$+\frac{\Delta t}{r_{i+\frac{1}{2}}}D_r^+\mu_z^+\left\{r_i\left[-u_{i,j}^{n+\frac{1}{2}}w_{i,j}^{n+\frac{1}{2}}+\frac{\nu}{2}w'_{i,j}\right]\right\}$$
$$+\frac{\Delta t}{r_{i+\frac{1}{2}}}D_z^+\mu_r^+\left\{r_i\left[-(w_{i,j}^{n+\frac{1}{2}})^2+\frac{\nu}{2}w_{i,j}^{\backslash}\right]\right\}$$
$$+\frac{\Delta t}{r_{i+\frac{1}{2}}}\mu_r^+\mu_z^+\left\{r_i\left[-G_z p_{i,j}^{n-\frac{1}{2}}\right]\right\},$$

where, for any staggered grid function $f_{i+\frac{1}{2},j+\frac{1}{2}}$, the discrete Laplacian operator $\nabla^2 f_{i+\frac{1}{2},j+\frac{1}{2}}$ is defined by

$$\nabla^2 f_{i+\frac{1}{2},j+\frac{1}{2}}\equiv\frac{1}{r_{i+\frac{1}{2}}}D_r^+r_iD_r^-f_{i+\frac{1}{2},j+\frac{1}{2}}+D_z^+D_z^-f_{i+\frac{1}{2},j+\frac{1}{2}}. \tag{26}$$

Once we obtain the cell averages of the provisional field $\bar{\mathbf{u}}^*_{i+\frac{1}{2},j+\frac{1}{2}}$, we need to convert this result back into point values $\mathbf{u}^*{}_{i+\frac{1}{2},j+\frac{1}{2}}$ at the staggered cells' centers. If the provisional field $\mathbf{u}^*(r,z)$ is approximated by a piecewise-linear function,

$$\mathbf{u}^*(r,z)=\mathbf{u}^*{}_{i+\frac{1}{2},j+\frac{1}{2}}+(\mathbf{u}^*)'_{i+\frac{1}{2},j+\frac{1}{2}}(r-r_{i+\frac{1}{2}})+(\mathbf{u}^*)^{\backslash}_{i+\frac{1}{2},j+\frac{1}{2}}(z-z_{j+\frac{1}{2}}),$$
$$(r,z)\in\mathcal{C}_{i+\frac{1}{2},j+\frac{1}{2}}, \tag{27}$$

then its cell averages are given by

$$\bar{\mathbf{u}}^*_{i+\frac{1}{2},j+\frac{1}{2}}=\mathbf{u}^*{}_{i+\frac{1}{2},j+\frac{1}{2}}+\frac{\Delta r^2}{12r_{i+\frac{1}{2}}}(\mathbf{u}^*)'_{i+\frac{1}{2},j+\frac{1}{2}}. \tag{28}$$

It is easily verified that $(\mathbf{u}^*)'_{i+\frac{1}{2},j+\frac{1}{2}} \approx (\bar{\mathbf{u}}^*)'_{i+\frac{1}{2},j+\frac{1}{2}}$ to second-order accuracy. Therefore the point values are recovered from the average values by

$$\mathbf{u}^*{}_{i+\frac{1}{2},j+\frac{1}{2}} = \bar{\mathbf{u}}^*_{i+\frac{1}{2},j+\frac{1}{2}} - \frac{\Delta r^2}{12 r_{i+\frac{1}{2}}} D_r^0 \bar{\mathbf{u}}^*_{i+\frac{1}{2},j+\frac{1}{2}}. \tag{29}$$

We note that this procedure may require some modification when limiters are present.

This concludes the second step of the calculation of the provisional field.

3.1.3. Hodge projection. The result obtained in the last section is a non–divergence-free provisional field $\mathbf{u}^*$. The third step accounts for incompressibility by extracting its divergence-free part. The remainder (irrotational) part is used to update the pressure gradient.

In differential form, the new flow field $\mathbf{u}^{n+1}$ needs to satisfy the incompressibility condition

$$\frac{1}{r}\frac{\partial}{\partial r}(r u^{n+1}) + \frac{\partial w^{n+1}}{\partial z} = 0. \tag{30}$$

As the central-differencing approach is based on cell averaging, we choose to impose the incompressibility condition in its integral form. Integrating the differential condition over the cell $\mathcal{C}_{i,j}$ we get

$$\Delta r\, D_r^- \int_{J_j} dz\, r_{i+\frac{1}{2}} u^{n+1}_{i+\frac{1}{2},j+\frac{1}{2}} + \Delta z\, D_r^- \int_{I_i} dz\, r_{i+\frac{1}{2}} w^{n+1}_{i+\frac{1}{2},j+\frac{1}{2}} = 0, \tag{31}$$

which is again approximated using the second-order trapezoidal rule. Thus the discrete form of the incompressibility condition is

$$D_r^- \mu_z^- \left(r_{i+\frac{1}{2}} u^{n+1}_{i+\frac{1}{2},j+\frac{1}{2}} \right) + D_z^- \mu_r^- \left(r_{i+\frac{1}{2}} w^{n+1}_{i+\frac{1}{2},j+\frac{1}{2}} \right) = 0. \tag{32}$$

We now perform a discrete Hodge decomposition. We decompose the provisional field $\mathbf{u}^*{}_{i+\frac{1}{2},j+\frac{1}{2}}$ into the sum of the updated flow field $\mathbf{u}^{n+1}_{i+\frac{1}{2},j+\frac{1}{2}}$ and the gradient of a scalar grid function $\phi_{i,j}$:

$$\begin{aligned} u^{*n+1}_{i+\frac{1}{2},j+\frac{1}{2}} &= u^{n+1}_{i+\frac{1}{2},j+\frac{1}{2}} + D_r^+ \mu_z^+ \phi_{i,j}, \\ l^{*n+1}_{i+\frac{1}{2},j+\frac{1}{2}} &= l^{n+1}_{i+\frac{1}{2},j+\frac{1}{2}}, \\ w^{*n+1}_{i+\frac{1}{2},j+\frac{1}{2}} &= w^{n+1}_{i+\frac{1}{2},j+\frac{1}{2}} + D_z^+ \mu_r^+ \phi_{i,j}. \end{aligned} \tag{33}$$

Up to the specification of boundary conditions (which are discussed in the next section), the substitution of the decomposition (33) into the discrete incompressibility condition (32) dictates the scalar potential $\phi_{i,j}$. It is the solution of the Poisson equation

$$\mu_z^+ \mu_z^- D_r^- \left(r_{i+\frac{1}{2}} D_r^+ \phi_{i,j} \right) + D_z^+ D_z^- \mu_r^- \left(r_{i+\frac{1}{2}} \mu_r^+ \phi_{i,j} \right) = \rho_{i,j}, \tag{34}$$

where

$$\rho_{i,j} \equiv D_r^- \mu_z^- \left(r_{i+\frac{1}{2}} u^*{}_{i+\frac{1}{2},j+\frac{1}{2}} \right) + D_z^- \mu_r^- \left(r_{i+\frac{1}{2}} w^*{}_{i+\frac{1}{2},j+\frac{1}{2}} \right). \tag{35}$$

The calculation of $\phi_{i,j}$ allows the flow field to be updated from (33), and the pressure gradient is updated by

$$
\begin{aligned}
G_r p^{n+\frac{1}{2}}_{i+\frac{1}{2},j+\frac{1}{2}} &= \mu_r^+ \mu_z^+ G_r p^{n-\frac{1}{2}}_{i,j} + \tfrac{1}{\Delta t} D_r^+ \mu_z^+ \phi_{i,j}, \\
G_z p^{n+\frac{1}{2}}_{i+\frac{1}{2},j+\frac{1}{2}} &= \mu_r^+ \mu_z^+ G_z p^{n-\frac{1}{2}}_{i,j} + \tfrac{1}{\Delta t} D_z^+ \mu_r^+ \phi_{i,j}.
\end{aligned} \tag{36}
$$

This concludes the calculation of the time step.

The evolution of the flow field from time t^n to time t^{n+1} induces a spatial shift from the cells $\mathcal{C}_{i,j}$ to the staggered cells $\mathcal{C}_{i+\frac{1}{2},j+\frac{1}{2}}$. For successive steps, the method consists of alternations, every second step, between the two grids. Thus, the next step shifts back to the original grid. The calculations involved in the alternating steps are identical, up to a systematic interchange between forward and backward operators (e.g., $D_r^+ \leftrightarrow D_r^-$), and between the cell centers (r_i, z_j) and $(r_{i+\frac{1}{2}}, z_{j+\frac{1}{2}})$.

3.2. Boundary cells. The numerical scheme presented in the previous section remains to be adapted for the radial boundary cells $(0, j)$ and $(M-1, j)$. The alternation between the two grids requires special attention and, in particular, implies different treatments for odd and even time steps. As in the preceding section, we will describe the procedure only for time steps which start with the grid $\mathcal{C}_{i,j}$ and end with the staggered grid $\mathcal{C}_{i+\frac{1}{2},j+\frac{1}{2}}$.

We adopt the following convention: in the initial state, the left edge of the system ($r = r_L$) *intersects* the left boundary cells (i.e., $r_0 = r_L$), while the right edge of the system ($r = r_R$) *coincides* with the edge of the right boundary cells (i.e., $r_{M-1} = r_R - \frac{1}{2}\Delta r$). That is, the right boundary cells lie entirely inside the system, whereas only half of the left boundary cells do so. This situation is reversed in the succeeding time steps (see Fig. 3). This sets the grid spacing $\Delta r = (r_R - r_L)/(M - \frac{1}{2})$.

3.2.1. Piecewise-linear reconstruction. The piecewise-linear approximation $\mathbf{u}^n(r, z)$ assumes the same form (12) inside the boundary cells. The only modification is to the r-derivatives, which have to be calculated using second-order one-sided expressions:

$$
\begin{aligned}
\mathbf{u}'_{0,\cdot} &= -\frac{1}{2h}\left(3\mathbf{u}^n_{0,\cdot} - 4\mathbf{u}^n_{1,\cdot} + \mathbf{u}^n_{2,\cdot}\right), \\
\mathbf{u}'_{M-1,\cdot} &= \frac{1}{2h}\left(3\mathbf{u}^n_{M-1,\cdot} - 4\mathbf{u}^n_{M-2,\cdot} - \mathbf{u}^n_{M-3,\cdot}\right).
\end{aligned} \tag{37}
$$

3.2.2. Calculation of the provisional field. As described in section 3.1.2, the calculation of the provisional field consists of three steps: (i) a predictor to estimate $\mathbf{u}^{n+\frac{1}{2}}_{i,j}$; (ii) a corrector to calculate the cell averages of the provisional field $\bar{\mathbf{u}}^*_{i+\frac{1}{2},j+\frac{1}{2}}$; and (iii) an interpolation which recovers point values of the provisional field $\mathbf{u}^*{}_{i+\frac{1}{2},j+\frac{1}{2}}$.

The predictor field $\mathbf{u}^{n+\frac{1}{2}}_{i,j}$ is calculated at the centers of the cells $\mathcal{C}_{i,j}$. The right boundary cells ($i = M-1$) lie entirely inside the system and can follow exactly the same treatment as the interior cells (25), with the derivative operators replaced by one-sided stencils. The centers of the left boundary cells ($i = 0$) are on the boundaries, and fields' values at those points are determined by the boundary conditions $\mathbf{u}^{n+\frac{1}{2}}_{0,\cdot} = \mathbf{u}(r_L)$. This situation is reversed in the corrector step, where the provisional field is calculated at the centers of the cells $\mathcal{C}_{i+\frac{1}{2},j+\frac{1}{2}}$. Then left boundary cells are treated as interior cells while $\mathbf{u}^*{}_{M-1,\cdot} = \mathbf{u}(r_R)$.

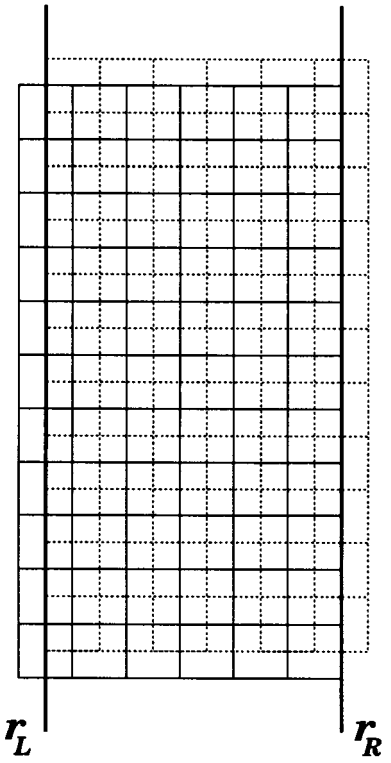

FIG. 3. *The computational grid and the physical domain. The solid (dotted) grid corresponds to the initial state for odd (even) time steps.*

3.2.3. Hodge projection. The Hodge projection decomposes the provisional field $\mathbf{u}^*$ into a divergence-free field $\mathbf{u}^{n+1}$ and an irrotational field (33). In the continuum case only the normal component of the divergence-free part can be specified as $u^{n+1}(r_L) = u^{n+1}(r_R) = 0$. In the discrete formulation it is possible within second-order accuracy also to impose constraints also on the tangential component w^{n+1}.

The flow fields $\mathbf{u}^*$ and $\mathbf{u}^{n+1}$ are given at the centers of the staggered cells $\mathcal{C}_{i+\frac{1}{2},j+\frac{1}{2}}$, while the scalar field $\phi_{i,j}$ is given at the centers of the original cells $\mathcal{C}_{i,j}$. At the left boundary ($i = 0$) the gradient of ϕ can be calculated using the same differencing stencil as in the interior cells. As the flow field itself is not calculated at the boundary, we will require that the *extrapolated* value of u^{n+1} vanishes at $r = r_L$, i.e.,

$$\frac{1}{8}\mu_z^+ \left(15u^{n+1}_{\frac{1}{2},\cdot} - 10u^{n+1}_{\frac{3}{2},\cdot} + 3u^{n+1}_{\frac{5}{2},\cdot}\right) = 0. \tag{38}$$

On the right side ($i = M - 1$) the flow field is calculated at the boundary. The fact that both $u^{n+1}_{i+\frac{1}{2},j+\frac{1}{2}}$ and $w^{n+1}_{i+\frac{1}{2},j+\frac{1}{2}}$ vanish at those points determines the form of the incompressibility condition with respect to the boundary cells $\mathcal{C}_{i,j}$:

$$-\frac{1}{\Delta r}\mu_z^+\mu_z^- D_r^-\phi_{i,j} + \frac{1}{2}D_z^+ D_z^-\mu_r^-\phi_{i,j} = -\frac{1}{\Delta r}\mu_z^- {u^*}_{i-\frac{1}{2},j+\frac{1}{2}} + \frac{1}{2}D_z^- {w^*}_{i-\frac{1}{2},j+\frac{1}{2}}. \tag{39}$$

(38) and (39) complete the specification of the boundary conditions for $\phi_{i,j}$.

We note that the Poisson equation defined by (34), (38), and (39) has a two-dimensional null space which corresponds to two additive constants, one for each of

TABLE 1

L_2-error and extrapolated convergence rates estimated from the comparison of 16×64, 32×128, and 64×256 grids. The parameters are $\eta = 0.883$, $H = 6$, $\omega = 0$, $\nu = 0.04$, and the total time is $t = 10$.

	$M = 16$, $N = 64$	Rate	$M = 32$, $N = 128$
$\|u_{M,N} - u_{2M,2N}\|_2$	$2.50 \cdot 10^{-3}$	1.98	$6.45 \cdot 10^{-4}$
$\|\ell_{M,N} - \ell_{2M,2N}\|_2$	0.23	1.95	$6.10 \cdot 10^{-2}$
$\|w_{M,N} - w_{2M,2N}\|_2$	$2.40 \cdot 10^{-3}$	1.93	$6.20 \cdot 10^{-4}$

two decoupled stencils ("checkerboard" pattern). These two degrees of freedom do not affect the values of the updated fields and therefore can be set arbitrarily.

4. Numerical results. We implemented the above central scheme. The implicit diffusion and Laplace equations were solved using the fast Fourier transform for the periodic z-axis. The time step was limited through the CFL stability condition, $\max(|u|/\Delta r, |w|/\Delta z)\,\Delta t < C$ where C is a constant. The CFL condition is a bound on the maximum distance along which information can propagate during a single time step. In our staggered central scheme it is essential that the characteristics emanating from the discontinuities between the piecewise-linear elements remain within the staggered cell, i.e., that the characteristics are not allowed to propagate by more than *half* a cell. This imposes the condition $C < \frac{1}{2}$. On the other hand, the constant C should be taken as large as possible in order to reduce the undesired numerical viscosity of the scheme. All our computations were carried out with $C = 0.45$. In cases where both $|u|$ and $|w|$ are everywhere small (i.e., when the flow is almost azimuthal), the time step has to be limited by the viscous terms. In view of the implicit Crank–Nicholson scheme used for the latter, this is more a matter of accuracy than stability. The code was implemented on a Sun Sparc Ultra-1 workstation. About 25% of the computing time was spent on the linear solvers required by the implicit diffusion scheme and by the projection. For a 32×1024 grid, each time step takes about 5 seconds. A typical run up to $t = 40$ takes less than two hours.

The parameters were chosen following the experimental study of [1]. The gap ratio $\eta = R_{in}/R_{out}$ was taken to be 0.883. The aspect ratio between the height of the cylinders and the gap width was taken to be $H = 32$, close to the experimental value of 30. Such an aspect ratio is a reasonable approximation of infinite cylinders. The parameter space was then explored by varying the two remaining parameters, ω and ν. The initial condition was the azimuthal Couette flow (10), added to a small random perturbation to allow the instability to develop. In most calculations we used $M = 32$ points in the radial direction and $N = 1024$ points in the axial direction.

To estimate the convergence rate we compared the solution with a solution obtained using twice as many grid points in each axis. The two calculations were then interpolated to a common grid using a third-order interpolation scheme. The L_2-norm of the difference was taken as an error estimate. Such error estimates are shown in Table 1 for a regime of parameters in which the initial Couette solution is unstable. The convergence rate was evaluated by Richardson extrapolation. The numbers indicate that the scheme is second-order accurate as claimed.

We first focus on flows where the outer cylinder does not rotate: $\omega = 0$ (and $\mathcal{R}_{out} = 0$). For large enough values of the viscosity ν (or low enough values of $\mathcal{R}_{in}$), the initial perturbation decays and the solution tends back to the azimuthal Couette flow. Below a critical value of $\nu \approx 0.0617$ the Couette solution is unstable and the perturbation grows until a new stationary state is eventually reached. This state is the

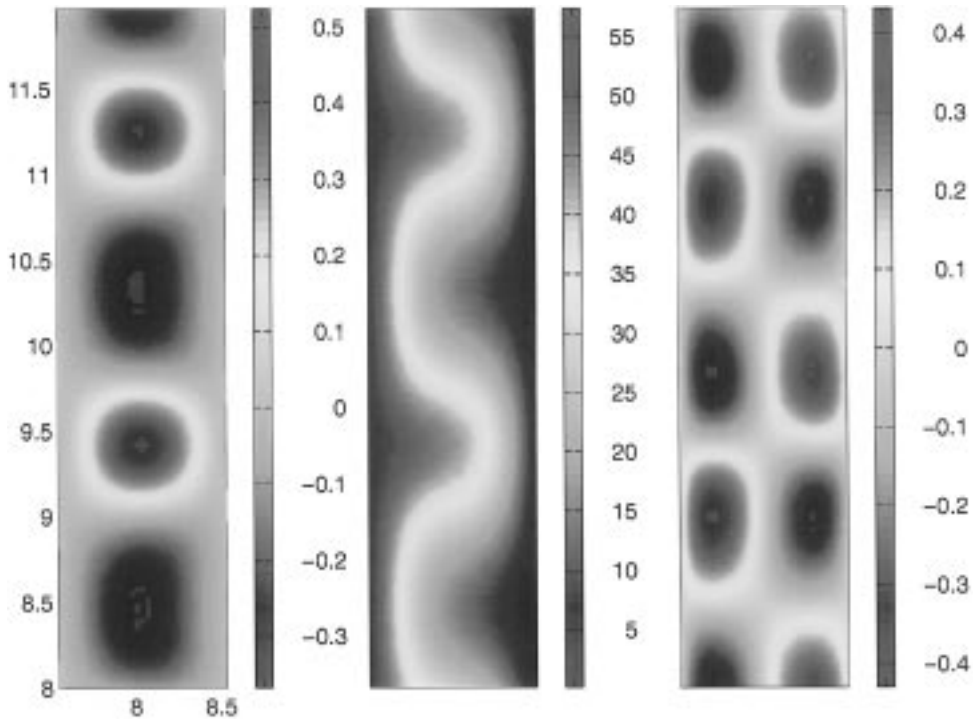

FIG. 4. *Color-level image of the flow components, u (left), ℓ (center), and w (right). The axes are the radial and the axial coordinates, and include a part of the cylindrical section. The parameters are $\omega = 0$ and $\nu = 0.03$.*

well-known Taylor vortices, a cellular structure of superimposed azimuthal vortices. A color-scale image of the three velocity components for the stationary Taylor vortices is shown in Fig. 4. An arrow representation of the (u, w) vector field is shown in Fig. 5. The axial segment corresponds to one wavelength which equals approximately two gap units.

For even lower values of $\nu \lesssim 0.04$ Taylor vortices are unstable and the resulting long-time behavior is no longer stationary. A transition to a new state of wavy vortices is observed in experiments. Such flow is not axisymmetric and therefore cannot be resolved by the present calculation.

The primary quantitative test of our results is a comparison of the instability growth rate with the prediction of linear stability theory. The linear stability calculation refers to the early evolution of a small perturbation about the steady Couette flow of the form

$$\delta\mathbf{u}(r, z, t) = \delta\mathbf{u}(r)\, e^{ikz}\, e^{\sigma t}, \tag{40}$$

where k is the axial wave number and σ is the amplification rate. The dispersion relation $\sigma(k)$ is a solution of the following eigenvalue problem [4]:

$$\begin{aligned} &\left(\frac{\partial}{\partial r}\frac{1}{r}\frac{\partial}{\partial r}r - k^2 - \frac{\sigma}{\nu}\right)\left(\frac{\partial}{\partial r}\frac{1}{r}\frac{\partial}{\partial r}r - k^2\right)\delta u = \frac{2k^2}{\nu}\left(A + \frac{B}{r^2}\right)\delta v, \\ &\left(\frac{\partial}{\partial r}\frac{1}{r}\frac{\partial}{\partial r}r - k^2 - \frac{\sigma}{\nu}\right)\delta v = \frac{2A}{\nu}\,\delta u, \end{aligned} \tag{41}$$

where δu, δv, and $\delta u'$ vanish at the boundaries.

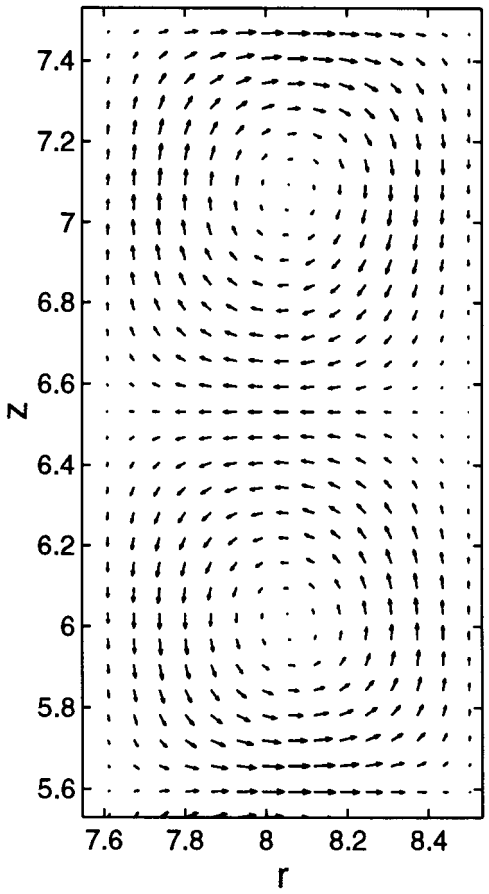

FIG. 5. *The (u, w) vector field: one wavelength showing a pair of counterrotating vortices.*

A perturbation mode k is unstable if $\sigma(k) > 0$. For low enough values of $\mathcal{R}_{in}$, all modes are stable. Above the transition point, there exists a continuum of unstable modes, which is reduced to a discrete spectrum in a finite periodic system.

To obtain a quantitative comparison between the simulation results and the linear stability equation, we recorded the time evolution of a specific axial Fourier mode k of the flow field at a fixed radial location (i.e., we fixed the radial index i and Fourier-transformed $\mathbf{u}_{i,j}$ with respect to the axial index j). Except for the early stages, $t \lesssim 1$, all such Fourier modes grow nearly exponentially before saturating. Nonlinear effects become noticeable only close to saturation. This procedure allowed us to compute the amplification rate associated with a wave number k.

In parallel, we discretized and solved the eigenvalue equation (41). Both procedures give amplification rates which depend on the grid sizes used in their calculations. We then performed successive grid refinements along with a Richardson extrapolation to estimate the amplification rates in the limit of an infinitely fine grid. A comparison between the two calculations is shown in Table 2. These results refer to the wavenumber $k = \pi$. The extrapolated values of the amplification rates σ are in excellent agreement to almost four significant digits.

TABLE 2

Amplification rates associated with the axial Fourier mode $k = \pi$ as a function of the viscosity ν. The fixed parameters are $\eta = 0.883$, $H = 6$, and $\omega = 0$. The set of results on the left refers to our numerical simulations using 32×128 and 64×256 grids; the third column is the extrapolated value. The set of results on the right refers to the linear stability calculation using 32 and 48 discretization points; the third column gives again the extrapolated value.

	Simulation			Linear stability		
ν	32×128	64×256	extrapolation	32	48	extrapolation
0.050	0.3134	0.3154	0.3161	0.3054	0.3113	0.3160
0.055	0.1795	0.1813	0.1819	0.1716	0.1773	0.1818
0.058	0.0998	0.1015	0.1021	0.0916	0.0974	0.1020

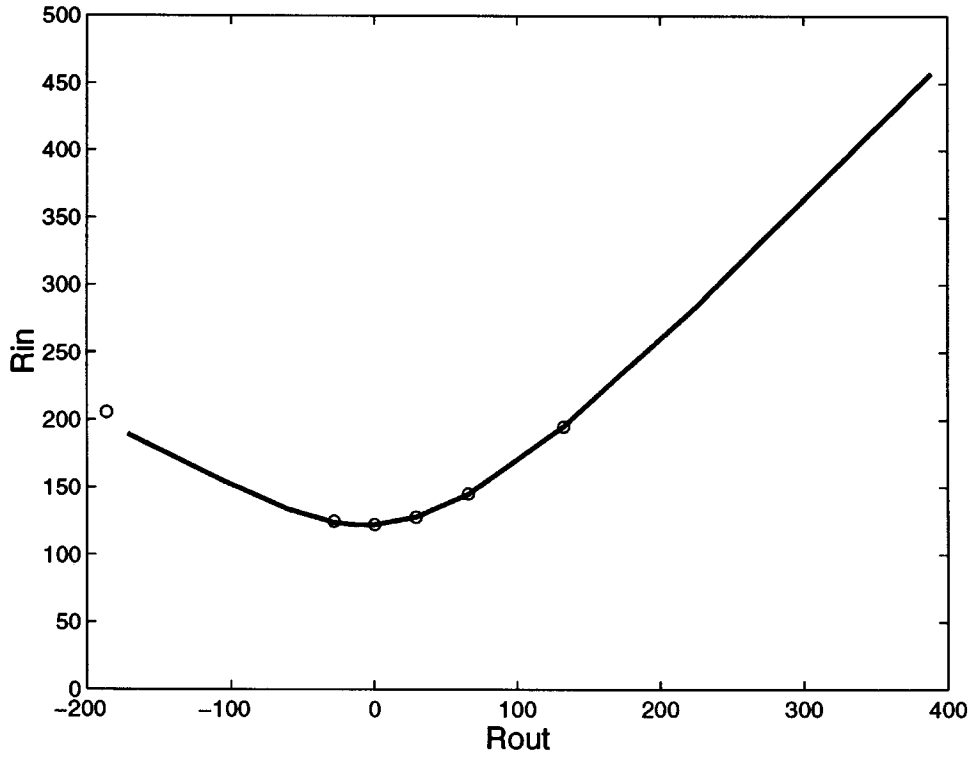

FIG. 6. *The neutral stability curve on the $\mathcal{R}_{in}$–$\mathcal{R}_{out}$ plane. The circles are the simulation results and the solid line is the linear stability calculation.*

We next considered the more general case where both cylinders rotate. The instability threshold, or the neutral stability curve, can be drawn on the $\mathcal{R}_{in}$–$\mathcal{R}_{out}$ plane. This curve is plotted in Fig. 6. The dots are the simulation results and the solid line is the linear stability calculation. The agreement is again good.

The instability threshold and the amplification rate of the perturbation both reflect properties of the flow in the linear regime where the velocity is almost azimuthal. The numerical scheme was also tested in a nonlinear regime by measuring the torque that the fluid exerts on one of the cylinders. The torque applied on the inner cylinder is given by

$$\tau = 2\pi\nu r_{in}^2 \int dz \left(2\frac{\ell}{r^2} - \frac{1}{r}\frac{\partial \ell}{\partial r} \right). \tag{42}$$

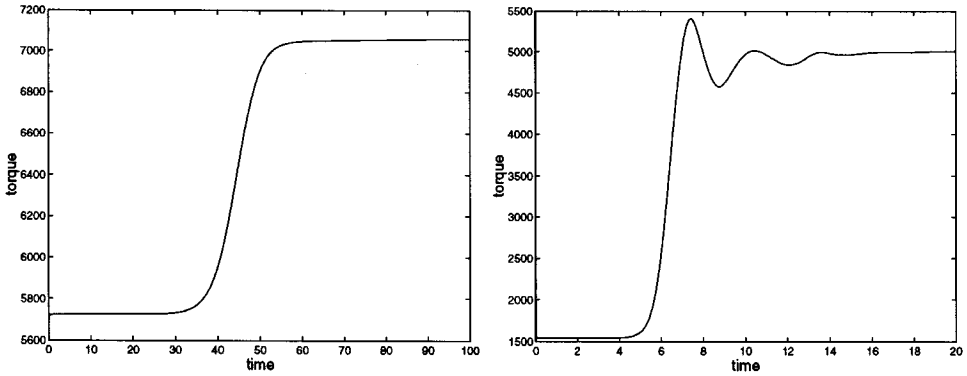

FIG. 7. *The torque exerted on the inner cylinder versus time. The parameters are* $\eta = 0.883$, $H = 32$, $\omega = 0$, $\nu = 0.05$ *(left), and* $\nu = 0.015$ *(right).*

We recorded the torque as a function of time. Results are shown in Fig. 7. Fig. 7a corresponds to the regime of steady Taylor cells. The torque monotonically increases from its Couette flow value toward its new steady value. Fig. 7b refers to a lower value of viscosity for which there is no steady flow. In this regime the torque overshoots and oscillates before decaying to a constant value. We remind the reader that our simulations are unable to properly describe this regime. Nonetheless oscillations in the torque evolution seem to coincide with the breakdown of the Taylor cells.

The torque is easily calculated for the azimuthal Couette flow and is given by

$$\tau = 4\pi\nu H \frac{(1-\omega)\eta^2}{(1-\eta)^2(1-\eta^2)}. \tag{43}$$

The torque is proportional to the viscosity of the fluid (the Couette cell was originally designed as an apparatus for measuring viscosity). This motivates the following definition of an *effective viscosity*:

$$\nu_{\text{eff}} \equiv \frac{(1-\eta)^2(1-\eta^2)}{4\pi H(1-\omega)\eta^2}\tau. \tag{44}$$

In Fig. 8 we plot the effective viscosity ν_{eff} versus the actual viscosity ν. The solid line is the Couette flow solution. For viscosity smaller than the instability threshold $\nu \approx 0.0617$, the effective viscosity is larger than the actual one. The effective viscosity increases as the viscosity is further reduced and reaches a maximum for $\nu \approx 0.044$.

5. Conclusions. We presented a numerical study of the axisymmetric Couette–Taylor problem, using a scheme based on the KT scheme [14]. The new scheme is a second-order central scheme combined with the projection method. While almost as accurate as modern upwind schemes, the new scheme proved to be more robust against the formation of spurious vortical structures, and above all it is very simple. In particular, it is Riemann-solver-free and does not require any of the flux limiter methodology.

The simplicity of the KT scheme makes it easy to generalize and adapt for tackling new problems. This is demonstrated in this paper where we apply the method on a cylindrical geometry. The crucial step in the adaptation to a new coordinate system is to formulate the equations of motion in the appropriate conservative form;

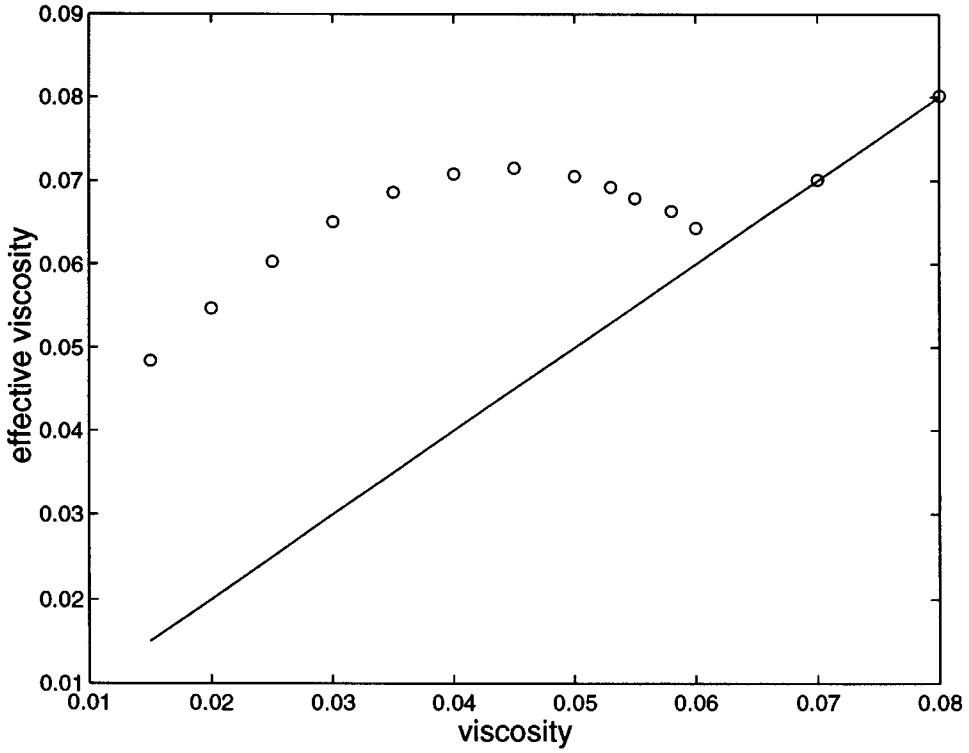

FIG. 8. *The effective viscosity versus the actual viscosity for* $\eta = 0.883$, $H = 32$, *and* $\omega = 0$. *The straight line is the functional dependence for Couette flow.*

the coordinate system imposes the representation of the divergence operator and thus the form of the corresponding fluxes. Once the equations have been written in conservative form, the derivation of the three steps—the piecewise-linear reconstruction, the calculation of the provisional field, and the Hodge projection—is just a matter of simple and straightforward algebra.

The treatment of boundary conditions fits naturally into this framework. The alternation between two computational grids implies that each perimeter cell is alternately entirely inside the system or intersected by the interface. In the first case, perimeter cells follow the same treatment as interior cells except for the use of one-sided stencils to calculate derivatives. In the second case, the center of the perimeter cells is at the interface and the boundary conditions are imposed directly.

In the Taylor cell regime, the early stages of the instability were compared to the predictions of linear stability theory. The agreement was excellent, and when properly extrapolated the results agree to the fourth significant digit. Nonlinear properties were also tested by performing torque measurements.

This study shows that the new central scheme makes possible the computation of flow problems with significantly less effort than with a comparable upwind scheme. Simplicity and adaptivity are the virtues that make this approach potentially adequate for solving more complex problems such as the flow of non-Newtonian fluids. A study of such systems is in progress [13].

Acknowledgments. I have benefited from fruitful discussions with A. Chorin, M. Denn, A. Kast, D. Levy, P. Marcus, S. Muller, D. Nolan, H. Swinney, and E. Tadmor. I thank A. Chorin and A. Kast for a critical reading of the manuscript.

REFERENCES

[1] C.D. Andereck, S.S. Liu, and H.L. Swinney, *Flow regimes in a circular Couette system with independently rotating cylinders*, J. Fluid Mech., 164 (1985), pp. 155–183.
[2] J.B. Bell, P. Colella, and H.M. Glaz, *A second order projection method for the incompressible Navier-Stokes equations*, J. Comput. Phys., 85 (1989), pp. 257–283.
[3] D.L. Brown and M.L. Minion, *Performance of under-resolved two-dimensional incompressible flow simulations*, J. Comput. Phys., 122 (1995), pp. 165–183.
[4] S. Chandrasekhar, *Hydrodynamics and Hydromagnetic Stability*, Dover, New York, 1961.
[5] A.J. Chorin, *On the convergence of discrete approximations to the Navier-Stokes equations*, Math. Comput., 22 (1969), pp. 745–762.
[6] P. Colella and E.G. Puckett, *Modern Numerical Methods for Fluid Flow*, in preparation.
[7] P. Colella and P. Woodward, *The piecewise parabolic method (PPM) for gas-dynamical simulations*, J. Comput. Phys., 54 (1984), pp. 174–201.
[8] W. E and C.-W. Shu, *A numerical resolution study of high-order essentially non-oscillatory schemes applied to incompressible flow*, J. Comput. Phys., 110 (1993), pp. 39–46.
[9] S.K. Godunov, *A finite difference method for the numerical computation of discontinuous solutions of the equations of fluid dynamics*, Mat. Sb., 47 (1959), pp. 271–290.
[10] E. Godlewski and P.-A. Raviart, *Hyperbolic Systems of Conservation Laws*, Math. Appl., Ellipses, Paris, 1991.
[11] A. Harten, *ENO schemes with subcell resolution*, J. Comput. Phys., 83 (1989), pp. 148–184.
[12] G.S. Jiang and E. Tadmor, *Non-oscillatory central schemes for multidimensional hyperbolic conservation laws*, SIAM J. Sci. Comput., in press.
[13] R. Kupferman, *Simulation of Viscoelastic Fluids: Couette-Taylor flow*, LBNL report 40302, Lawrence Berkeley National Laboratory, Berkeley, CA, 1997.
[14] R. Kupferman and E. Tadmor, *A fast high-resolution second-order central scheme for incompressible flows*, Proc. Nat. Acad. Sci. U.S.A., 94 (1997), pp. 4848–4852.
[15] P.D. Lax, *Weak solutions of non-linear hyperbolic equations and their numerical computations*, Comm. Pure Appl. Math., 7 (1954), pp. 159–193.
[16] B. van Leer, *Towards the ultimate conservative difference scheme. V. A second order sequel to Godunov's method*, J. Comput. Phys., 32 (1979), pp. 101–136.
[17] R.J. LeVeque, *Numerical Methods for Conservation Laws*, Birkhäuser-Basel, Switzerland, Verlag, 1992.
[18] D. Levy and E. Tadmor, *Non-oscillatory central schemes for the incompressible 2-D Euler equations*, Math. Res. Lett., 4 (1997), pp. 1–20.
[19] X.-D. Liu and S. Osher, *Nonoscillatory high order accurate self-similar maximum principle satisfying shock capturing. I.*, SIAM J. Numer. Anal., 33 (1996), pp. 760–779.
[20] X.-D. Liu and E. Tadmor, *Third order nonoscillatory central scheme for hyperbolic conservation laws*, Numer. Math., 79 (1998), pp. 397–425.
[21] H. Nessyahu and E. Tadmor, *Non-oscillatory central differencing for hyperbolic conservation laws*, J. Comput. Phys., 87 (1990), pp. 408–463.
[22] S. Osher, *Riemann solvers, the entropy condition, and difference approximations*, SIAM J. Numer. Anal., 21 (1984), pp. 217–235.
[23] Lord Rayleigh, *On the dynamics of revolving fluids*, Sci. Papers, 6 (1920), pp. 447–453.
[24] P. Roe, *Approximate Riemann solvers, parameter vectors, and difference schemes*, J. Comput. Phys., 43 (1981), pp. 357–372.
[25] R. Sanders and A. Weiser, *High resolution staggered mesh approach for nonlinear hyperbolic systems of conservation laws*, J. Comput. Phys., 101 (1992), pp. 314–329.
[26] P.K. Sweby, *High resolution schemes using flux limiters for hyperbolic conservation laws*, SIAM J. Numer. Anal., 21 (1984), pp. 995–1011.
[27] E. Tadmor and C.C. Wu, *Central scheme for the multidimensional MHD equations*, in preparation.